NANO · MICRO small
www.small-journal.com

Freestanding 1T-$Mn_xMo_{1-x}S_{2-y}Se_y$ and $MoFe_2S_{4-z}Se_z$ Ultrathin Nanosheet-Structured Electrodes for Highly Efficient Flexible Solid-State Asymmetric Supercapacitors

Uday Narayan Pan, Vikas Sharma, Tolendra Kshetri, Thangjam Ibomcha Singh, Dasu Ram Paudel, Nam Hoon Kim, and Joong Hee Lee**

Fabrication of hierarchical nanosheet arrays of 1T phase of transition-metal dichalcogenides is indeed a critical task, but it holds immense potential for energy storage. A single-step strategy is employed for the fabrication of stable 1T-$Mn_xMo_{1-x}S_{2-y}Se_y$ and $MoFe_2S_{4-z}Se_z$ hierarchical nanosheet arrays on carbon cloth as positive and negative electrodes, respectively. The flexible asymmetric supercapacitor constructed with these two electrodes exhibits an excellent electrochemical performance (energy density of ≈69 Wh kg^{-1} at a power density of 0.985 kW kg^{-1}) with ultralong cyclic stability of ≈83.5% capacity retention, after 10 000 consecutive cycles. Co-doping of the metal and nonmetal boosts the charge storage ability of the transition-metal chalcogenides following enrichment in the metallic 1T phase, improvement in the surface area, and expansion in the interlayer spacing in tandem, which is the key focus of the present study. This study explicitly demonstrates the exponential enhancement of specific capacity of MoS_2 following intercalation and doping of Mn and Se, and Fe_2S_3 following doping of Mo and Se could be an ideal direction for the fabrication of novel energy-storage materials with high-energy storage ability.

1. Introduction

Pseudocapacitive energy-storage systems like supercapacitors are highly influenced by the composition, shape, size, conductivity, and the structure of their respective electrode materials.[1–3] The ever-increasing energy demand has posed an alarming situation for developing novel and efficient materials to achieve high power and energy density energy-storage devices. Moreover, with the introduction of flexible electronics, it has become necessary to fabricate devices that are handy, shock-resistant, space-confined, and also foldable without compromising the performance.[1–5] As the pseudocapacitors involve a large number of simultaneous redox reactions, stable and efficient morphologies of electrode materials with high conductivity become extremely critical for long-term stability of the devices.[1–5] To achieve this, a deep insight into the materials chemistry is required with which tunable morphologies with high surface area, conductivity, and porosity can be achieved.[1–5] Therefore, to meet the per-capita energy requirement, large-scale commercialization of generated energy and the demand for wearable consumable electronics such efficient energy-storage devices equipped with high surface-area electrode materials have become critically important.[1–5]

Transition-metal chalcogenides (TMCs) have recently been proposed for energy storage because of their exclusive physical and chemical characteristics, which include high conductivity, high specific capacity, large surface area, thermal and chemical durability, and high cyclic stability.[1–13] Among different TMCs, transition-metal dichalcogenides (TMDCs) of molybdenum (Mo), tungsten (W), and tin (Sn) have been studied as the positive-electrode material and the sulfides of iron as the negative electrode energy-storage materials, respectively, because of their appreciable conductivity and specific capacities.[6–15] However, the currently developed and utilized TMCs for supercapacitors do not meet the existing demand of the energy industry, because of their poor charge-holding capacity, which limits their energy and power densities. This provides a unique window for further improvement on charge-storage performance of the TMCs following tuning their morphology and band gap.

Among all the TMDCs, MoS_2 is chemically and physically the most stable, with ample abundance in the Earth's crust. Therefore, it becomes a cheap and easily available alternative for various applications, such as energy storage, flexible electronics, and other electrical and optical applications.[6–15] The MoS_2 framework contains a central Mo atom sandwiched between two S atoms, which leads to the development of S–Mo–S

Dr. U. N. Pan, Dr. V. Sharma, Dr. T. Kshetri, T. I. Singh, D. R. Paudel, Prof. N. H. Kim, Prof. J. H. Lee
Advanced Materials Institute of BIN Convergence Technology and Department of BIN Convergence Technology
Jeonbuk National University
Jeonju, Jeonbuk 54896, Republic of Korea
E-mail: nhk@jbnu.ac.kr; jhl@jbnu.ac.kr
Prof. J. H. Lee
Carbon Composite Research Centre
Department of Polymer-Nano Science and Technology
Jeonbuk National University
Jeonju, Jeonbuk 54896, Republic of Korea
The ORCID identification number(s) for the author(s) of this article can be found under https://doi.org/10.1002/smll.202001691.

DOI: 10.1002/smll.202001691

triple atomic planes. These S–Mo–S planes remain packed by van der Waals forces that stabilize a 2D lamellar structure. Due to the variations in the arrangement of the sulfur atoms in the S–Mo–S triple atomic plane, the monolayer of MoS_2 shows polymorphism. MoS_2 exhibits two distinct crystal phases with completely different electronic structures: 2H phase (semiconducting) and 1T phase (metallic).[6–15] Although the 1T phase of MoS_2 displays high electronic conductivity and fast charge transfer, its poor thermodynamic stability and tedious synthesis process kept it largely ignored in energy-storage applications.[6–15] The 1T phase is generally stabilized with the intercalation of a second metal ion, such as Li/K/Mn, as electron donor in the host phase.[6–15] Mn, among all, has the highest affinity toward sulfur and forms a stable strong bond in zinc-blende, rock salt, or wurtzite structures, and also possesses antiferromagnetic coupling with neighboring S atom when doped in MoS_2[6–15] Thus, Mn can be an ideal dopant for the stabilization of the 1T phase of MoS_2 in a hierarchical nanostructure.

On the other hand, nonmetal doping on MoS_2 expands the interlayer spacing, which increases the number of exposed active sites for electrochemical reactions and also allows directional passage of the electrolytic ions. With this, a significant enhancement in the charge-transfer kinetics is expected in these doped structures in comparison to the pristine MoS_2.[16–18] Among the various nonmetals, theoretical studies have predicted that chemical doping of selenium (Se) on MoS_2 is thermodynamically favorable and can significantly alter the electronic structure, especially the band gap, which is an important factor for the improvement of the energy storage and catalytic performance of MoS_2.[19,20] Moreover, as it is large in size, Se can also significantly increase the interlayer spacing of MoS_2.[16–20] Therefore, we can conclude from the discussion so far that the strategy of co-doping of metal and nonmetal on MoS_2 holds a high potential for significant improvement in the energy-storage characteristics. Likewise, although the Fe_2S_4 has been investigated as the negative electrode material for the supercapacitor, its electrochemical performance remains limited due to its moderate rate capability, poor cycling stability, and low specific capacity.[21–23] Hence, it is essential to improve the energy-storage performance of Fe_2S_4, which is possible by the same strategy involved in doping of other metals and nonmetals, as discussed previously for positive electrode.[21–23]

Apart from the inherent electronic structure, other important parameters like surface area and porosity also determine the fate of the electrochemical performance of the electrodes.[1–13] Various nanostructures of MoS_2 or Fe_3S_4 have been synthesized and reported to date, such as nanosheets, nanorods, nanoparticles, or nanowires.[6–9,14–18,21–26] Unfortunately, most of them, with high surface area and porosity, are synthesized in powdered form, which requires binders and conductive materials as additives for use as electrodes in supercapacitors. The additional components increase the equivalent series resistance (ESR), leading to mediocre performances of the electrode. Freestanding electrodes, in which materials are grown directly on the current-collecting substrate, can resolve the issues related to the shortfalls caused by such external additives.[12–23] In the present study, carbon cloth (CC) is chosen as current collecting substrate because of its super flexibility, high conductivity, excellent mechanical strength, high porosity, high corrosion resistivity, light weight, and ease of comprehensive commercialization. Typical metallic substrates like copper or aluminum foil or nickel foam are not used, because of their rigid nature that does not satisfy the scope of the present study dealing with development of flexible devices.[4,5,21–23] In the end, issues about the leakage of the electrolyte and the gradual leaching and detachment of the active material from the current collector are tackled by using the gel electrolyte.[21–23,26]

Herein, we report the fabrication of a flexible and highly efficient electrode based on the ultrathin hierarchical and porous nanosheet structure of 1T-$Mn_xMo_{1-x}S_{2-y}Se_y$ and $MoFe_2S_{4-z}Se_z$ developed via a single-step, easy, and scalable hydrothermal approach. The present work is aimed at boosting the specific capacity of MoS_2 following enrichment of the 1T phase, increasing the interlayer spacing and improving the surface morphology by intercalation of Mn and Se. Typically, the metallic 1T phase holds a high potential for boosting the specific capacity of pristine MoS_2 because of its very high electrical conductivity. But no significant effort has been made so far to fabricate the hierarchical 1T nanostructure of MoS_2 on a freestanding current-collecting substrate. In this study, we have tried to address this issue for the first time to the best of our knowledge and fabricated a highly stable ultrathin 1T MoS_2 nanosheet on a flexible carbon-cloth substrate following intercalation and doping of Mn and Se. The chemistry involved and the reasons for using this strategy are discussed elaborately in this paper. The as-fabricated material showed an exceptional increase in the specific and areal capacity compared to pristine MoS_2. Similarly, a flexible negative electrode was also fabricated following the doping of Mo and Se on Fe_3S_4. As MoS_2 and $MoSe_2$ are known to exhibit a stable sheet structure, incorporation of Mo and Se simultaneously on Fe_3S_4 has helped in the growth of ultrathin hierarchical nanosheets on flexible CC showing high specific capacity, as electrodes.[6–15,19,20] Finally, a highly flexible solid state asymmetric supercapacitor (FS-ASC) was fabricated following assembling the 1T-$Mn_xMo_{1-x}S_{2-y}Se_y$ and $MoFe_2S_{4-z}Se_z$ ultrathin nanosheet-based flexible electrodes using gel electrolyte. The as-prepared FS-ASC showed exceptionally high energy density and cyclic stability with super flexibility. Thus, it is proposed that such systems can act as model systems for the ongoing research in the field of energy-storage devices.

2. Results and Discussion

2.1. Structural and Morphological Characterizations of 1T-$Mn_xMo_{1-x}S_{2-y}Se_y$ and $MoFe_2S_{4-z}Se_z$

For the synthesis of the flexible 1T-$Mn_xMo_{1-x}S_{2-y}Se_y$ and $MoFe_2S_{4-z}Se_z$ electrodes, we carried out a single-step direct growth approach. Typically, the ultrathin nanosheets were grown on carbon cloth following direct sulfurization of the precursor salts in a facile hydrothermal process. Different precursor salts were mixed in desired proportions with a clean carbon cloth submerged into the as-prepared solution, and a hydrothermal reaction was carried out at 180° for 14 h (**Scheme 1**; details are provided in the Experimental Section).[8,15,18,24] In order to achieve the ultrathin nanosheet structure of $Mn_xMo_{1-x}S_{2-y}Se_y$ with an enriched 1T phase, we

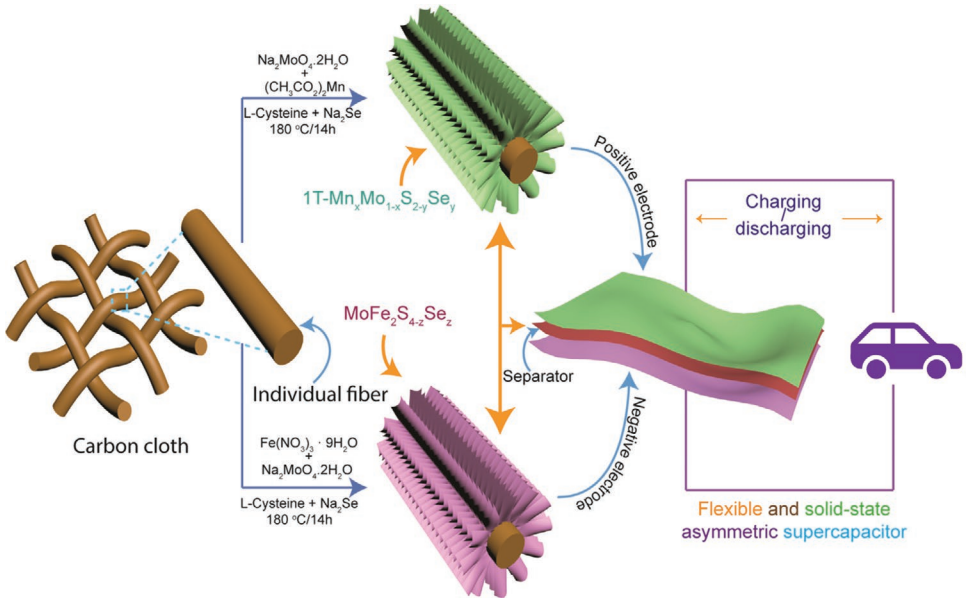

Scheme 1. Schematic illustration of the fabrication of a flexible and solid-state asymmetric supercapacitor (FS-ASC) based on 1T-$Mn_xMo_{1-x}S_{2-y}Se_y$ and $MoFe_2S_{4-z}Se_z$ hierarchical nanosheet arrays.

carried out a series of reactions. As per the literature, 10% Mn doping is optimal for the significant improvement in the optical and electrochemical performance of the bare MoS_2.[14] To eliminate any propensity in the formation of undesired MoS_2–MnS side product, we have chosen 1:9 mass ratio of the Mn and Mo precursor salts.[10,14,15] The morphological characterization of the as-synthesized material showed a slight improvement in the surface area and porosity after the intercalation of Mn on MoS_2 as observed from the Field emission scanning electron microscopic (FE-SEM) images and N_2 adsorption-desorption isotherms (Figures S1A,B and S2A, Supporting Information).

On the other hand, Se doping on MoS_2 is also considered as another effective approach for engineering the band gap of the host, which improves its conductivity and electrochemical performance.[19,20] The selenium doping also showed some improvement in the morphology, surface area, and porosity of the undoped MoS_2, as depicted from the FE-SEM and N_2 adsorption-desorption isotherms (Figures S1A,C and S2A, Supporting Information). Growth of an ultrathin sheet structure with a large surface area and good porosity was followed by co-intercalation of Mn and Se into the pristine MoS_2, as confirmed from the FE-SEM micrographs and N_2 adsorption-desorption isotherms (**Figure 1**A–C and **Figure 2**D).

Although, the growth of the sheet structure was observed for MoS_2, Mn-intercalated MoS_2, and Se-doped MoS_2, the excellence in terms of homogeneity, interconnection, and length of the sheets was nowhere near that of the $Mn_xMo_{1-x}S_{2-y}Se_y$ (Figure 1A–C and Figure S1, Supporting Information). This significant improvement in the morphology following the co-doping of Mn and Se could be attributed to the competing bond formation and coordination between like and unlike elements during the growth, which has a significant effect on the surface morphology.[10,14,15] The transmission electron microscopic (TEM) image (Figure 1D) revealed the highly wrinkled and furrowed structure indicating the large surface area and flexible nature of the material. The TEM image at the higher magnification (Figure 1E) showed the designated layered structure of the $Mn_xMo_{1-x}S_{2-y}Se_y$ with interlayer spacing ≈0.71 nm. The interlayer spacing was ≈15% higher than that in bulk MoS_2 (≈0.62 nm). This increase in the interlayer spacing following the formation of $Mn_xMo_{1-x}S_{2-y}Se_y$ ultrathin nanosheet was expected to raise the number of exposed active sites for electrochemical reactions.[10,16,17] Alongside, Se doping might also alter the electronic structure, which synergistically boosted the electrochemical reaction kinetics.[19,20] The high-resolution TEM (HRTEM) image of $Mn_xMo_{1-x}S_{2-y}Se_y$ (Figure 1F) and the corresponding inverse fast Fourier transform (IFFT) pattern (inset) showed lattice fringes with spacing ≈0.28 nm of the (100) plane for the $Mn_xMo_{1-x}S_{2-y}Se_y$ indicating the formation of the expected material.[10,13–18] The selected area electron diffraction (SAED) of the $Mn_xMo_{1-x}S_{2-y}Se_y$ (Figure S3, Supporting Information) also showed a diffraction pattern corresponding to the (100) and (110) planes of the $Mn_xMo_{1-x}S_{2-y}Se_y$ nanosheet arrays.[10,13–18] Elemental mapping of $Mn_xMo_{1-x}S_{2-y}Se_y$ obtained from both TEM (Figure 1G) and FE-SEM (Figure S4, Supporting Information) showed the presence of all the constituent elements Mo, S, Mn, and Se apparently in equivalent ratio.

X-ray photoelectron spectroscopy (XPS) analysis of the Mo 3d showed predominant enrichment of the 1T phase compared to that of the 2H phase (Figure 1H_1 and Figure S5, Supporting Information). The high-resolution XPS peaks at 231.6 eV (Mo $3d_{3/2}$) and 228.4 eV (Mo $3d_{5/2}$) corresponding to the 1T phase of the $Mn_xMo_{1-x}S_{2-y}Se_y$ showed much higher intensities compared to the peaks at 232.7 and 229.2 eV corresponding to the 2H phase.[10,13–18] Other peaks corresponding to Mo^{4+} and Mo^{3+} were also observed within the range of 240–226 eV. Figure 1H_2 represents the XPS spectrum regarding S 2p of $Mn_xMo_{1-x}S_{2-y}Se_y$ displayed peaks at 165.6, 163.4, 163.5, and 162.2 eV corresponding to the S 2p3/2 (2H), S 2p3/2 (1T), S 2p1/2 (2H), and S 2p1/2 (1T), respectively.[10,13–18] Figure 1H_3 represents the XPS spectrum corresponding to Mn 2p of $Mn_xMo_{1-x}S_{2-x}Se_x$ at

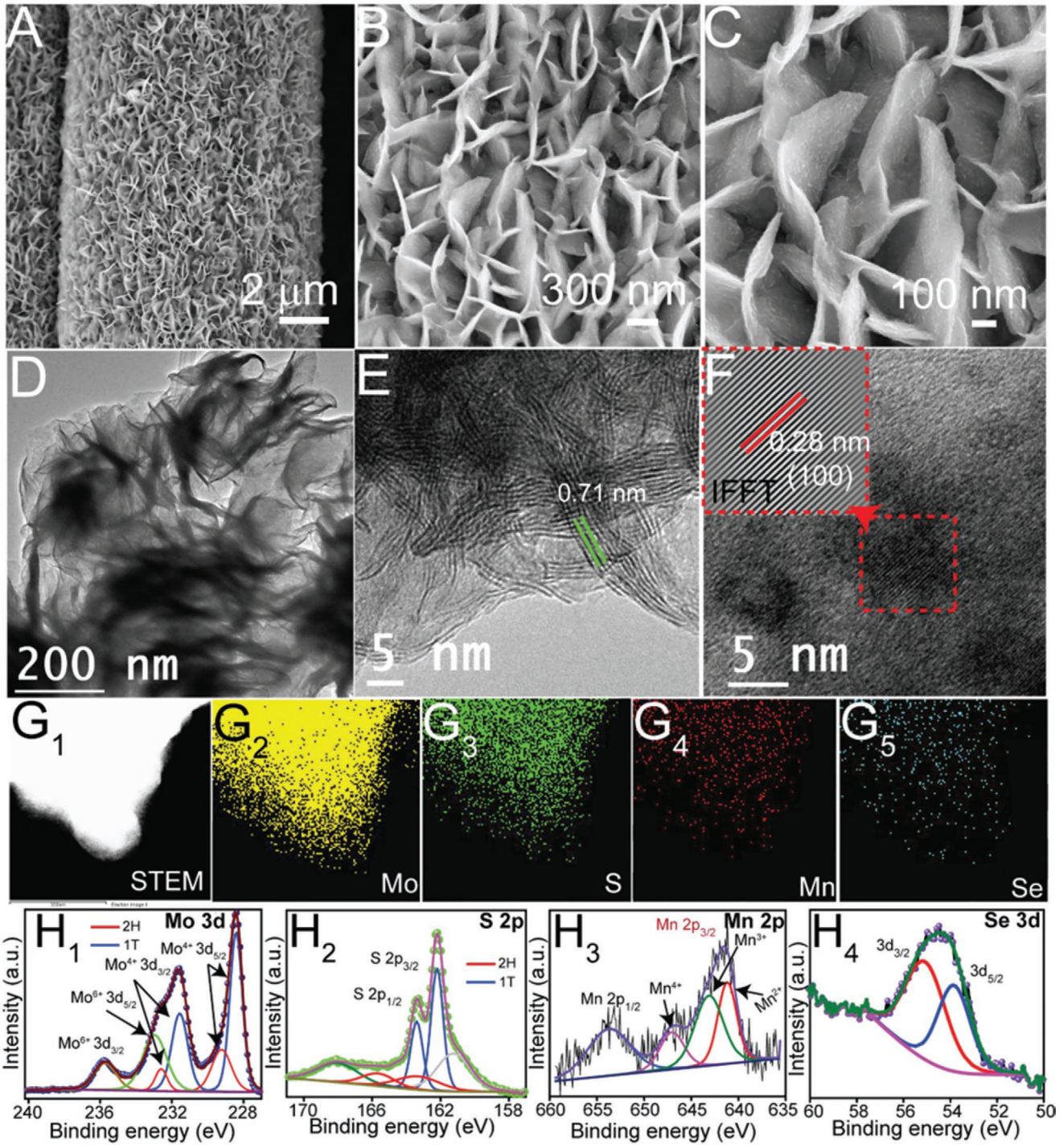

Figure 1. A–C) FE-SEM images at different magnifications (low to high) of 1T-$Mn_xMo_{1-x}S_{2-y}Se_y$ grown on carbon cloth, showing the ultrathin-sheet structures. D) TEM image of 1T-$Mn_xMo_{1-x}S_{2-y}Se_y$. E) Corresponding higher magnification TEM image showing the layered pattern. F) HRTEM image and corresponding IFFT pattern (inset) of 1T-$Mn_xMo_{1-x}S_{2-y}Se_y$. G_1) STEM image and corresponding elemental mapping of 1T-$Mn_xMo_{1-x}S_{2-y}Se_y$ showing the presence of individual constituent elements: G_2) molybdenum, G_3) sulfur, G_4) manganese, and G_5) selenium. H) High-resolution XPS spectrum of H_1) Mo 3d, H_2) S 2p, H_3) Mn 2p, and H_4) Se 3d.

a high resolution within the region 660-634 eV. The peaks at 653.2, 646.5, 643.1, and 641.1 eV could be attributed to the Mn $2p_{1/2}$, Mn $2p_{3/2}$ (of different oxidation states).[15,23] Figure $1H_4$ shows the high-resolution XPS spectrum for Se 3d within the region 50-60 eV. Peaks at 55.1 and 53.8 eV are assigned to $3d_{3/2}$ and $3d_{5/2}$ of Se 3d.[21–23,26] The above-discussed XPS results indicated the formation of 1T-$Mn_xMo_{1-x}S_{2-y}Se_y$ and were found in accordance with the other reported literatures.[10,13–18]

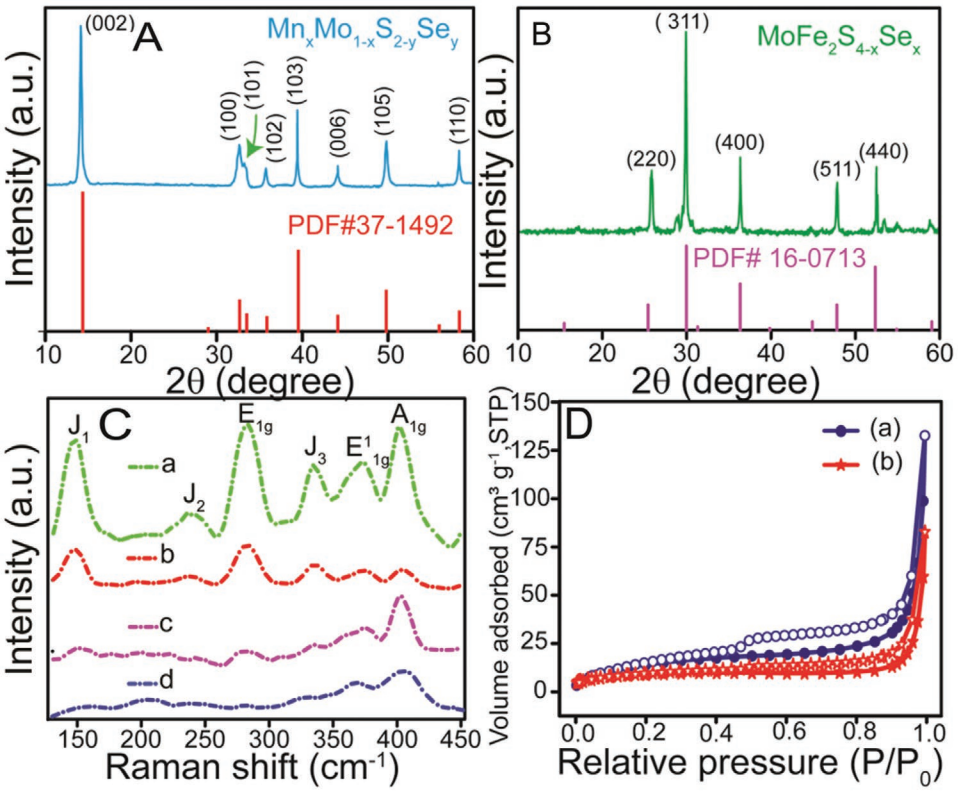

Figure 2. A) X-ray diffraction pattern of 1T-$Mn_xMo_{1-x}S_{2-y}Se_y$ nanosheets showing peaks at $2\theta = 14.2°$, 32.7°, 33.5°, 35.8°, 39.6°, 44.1°, 49.8°, and 58.3° corresponding to the (002), (100), (101), (102), (103), (006), (105), and (110) planes.[10,13–18] B) X-ray diffraction pattern of $MoFe_2S_{4-z}Se_z$ nanosheets showing peaks at $2\theta = 25.4°$, 30.1°, 36.4°, 48.1°, and 52.4° corresponding to the (220), (311), (400), (511), and (440) planes.[10,13–18] C) Raman spectra of a) 1T-$Mn_xMo_{1-x}S_{2-y}Se_y$, b) Mn-intercalated MoS_2, c) Se-doped MoS_2, and d) MoS_2 nanostructures, synthesized using the same method as described in the Experimental Section. D) N_2 adsorption-desorption isotherms of a) 1T-$Mn_xMo_{1-x}S_{2-y}Se_y$ and b) $MoFe_2S_{4-z}Se_z$ nanosheets.

The X-ray powder diffraction patterns of 1T-$Mn_xMo_{1-x}S_{2-y}Se_y$ (Figure 2A) showed peaks at 2θ = 32.7°, 33.5°, 35.8°, 39.6°, 44.1°, 49.8°, and 58.3° corresponding to the (100), (101), (102), (103), (006), (105), and (110) planes of $Mn_xMo_{1-x}S_{2-y}Se_y$ (PDF No. 37-1492).[10,13–18] The slight shift in the (002) peak from 14.4° to 14.2° in Figure 2A is due to enrichment of a metastable and highly conductive 1T phase of $Mn_xMo_{1-x}S_{2-y}Se_y$ as demonstrated in previously reported literature.[10] Raman analysis (Figure 2C) showed the peaks at 148, 242, 294, 336, 372, and 402 cm^{-1} corresponding to the J_1, J_2, E_{1g}, J_3, E^1_{2g}, and A_{1g} Raman modes, which were correlated to the 1T phase of the $Mn_xMo_{1-x}S_{2-y}Se_y$. The analysis of the Raman peaks of MoS_2 and Se-doped MoS_2 (Figure 2C) showed peaks at ≈400 and 375 cm^{-1} corresponding to the E^1_{2g} and A_{1g} Raman modes of the 2H phase of MoS_2. Alongside, the Mn-intercalated MoS_2 predominately showed the existence of the Raman peaks corresponding to 1T phase with relatively lower intensity than that of $Mn_xMo_{1-x}S_{2-y}Se_y$.[10,13–18] The Raman study conclusively showed the formation of a stable 1T-$Mn_xMo_{1-x}S_{2-y}Se_y$. "Mn" on the one side acts as an electron donor, while on the other side, Se assisted in the transversal displacement of S planes for the stabilization of the 1T phase.[10,13–18] These two doping together could possibly be responsible for the stabilization of the 1T phase of $Mn_xMo_{1-x}S_{2-y}Se_y$ in ultrathin nanosheet form.[10,13–18]

The superior porous nature and surface area of the 1T-$Mn_xMo_{1-x}S_{2-y}Se_y$ were determined from the N_2 adsorption–desorption isotherm (Figure 2D). The isotherm showed a type IV hysteresis loop, indicating the mesoporous nature of the material with specific surface area of ≈71 m^2 g^{-1} and average pore size of ≈14.5 nm (Figure 2D and Figure S2B, Supporting Information). The N_2 adsorption-desorption isotherm to MoS_2, Mn-intercalated MoS_2, and Se-doped MoS_2 showed much lower porosity to those of the 1T-$Mn_xMo_{1-x}S_{2-y}Se_y$ (Figure 2D and Figure S2A, Supporting Information) indicating an excellent surface structure of the ultrathin 1T-$Mn_xMo_{1-x}S_{2-y}Se_y$ for electrochemical reactions.[10,13–18]

Similarly, the negative electrode was designed following the doping of Mo and Se on Fe_3S_4. Fe_3S_4 does not possess any inherent sheet structure and has relatively low specific capacity. To boost its specific capacity/areal capacity involving the tuning of the electronic structure and surface morphology, Mo and Se were considered as ideal dopants for this purpose.[21–26] When Fe_3S_4 was grown on carbon cloth following the direct sulfurization of the iron nitrate in hydrothermal technique, no proper morphology of the material was observed (Figure S6A, Supporting Information). Se doping has slightly improved the loading of the material on the carbon cloth, but failed to achieve any distinguishable morphology with high surface area (Figure S6B, Supporting Information). Mo doping on Fe_3S_4, on the other hand, showed the initiation of a sheet structure, but

it was not sufficient to be claimed as an ultrathin sheet morphology with high surface area, which was actually the target of the present approach (Figure S6C, Supporting Information). Interestingly, the co-doping of the Mo and Se together on iron sulfide showed the growth of the ultrathin nanosheet structure exhibiting high specific surface area as confirmed from the FE-SEM images and nitrogen adsorption–desorption measurement (**Figure 3**A–C and Figure 2D). This was achieved

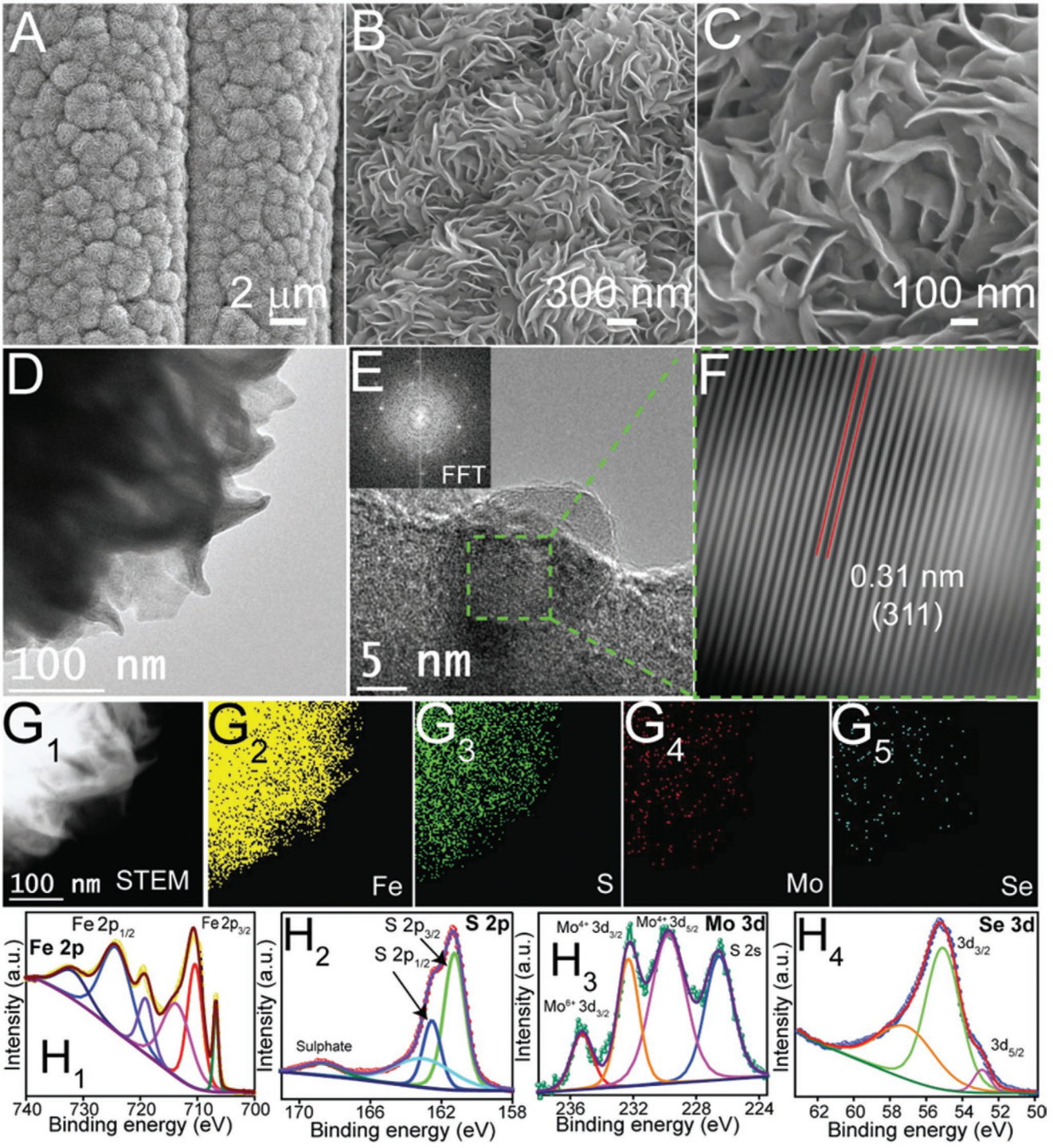

Figure 3. A–C) FE-SEM images at different magnifications (low to high) of $MoFe_2S_{4-z}Se_z$ grown on carbon cloth, showing the ultrathin-sheet structures. D) TEM image of $MoFe_2S_{4-z}Se_z$ confirming the sheet structure. E) HRTEM image, corresponding FFT pattern (inset) of $MoFe_2S_{4-z}Se_z$ nanosheets. F) Inverse fast Fourier transform of the corresponding HRTEM image clearly showing the lattice fringes of $MoFe_2S_{4-z}Se_z$. G_1) STEM image and corresponding elemental mapping of $MoFe_2S_{4-z}Se_z$ showing the presence of individual constituent elements: G_2) iron, G_3) sulfur, G_4) molybdenum, and G_5) selenium. H) High-resolution XPS spectrum of H_1) Fe 2p, H_2) S 2p, H_3) Mo 3d, and H_4) Se 3d.

because of the high propensity of MoS_2 and $MoSe_2$ to stabilize in the form of sheet structures. The FE-SEM images (Figure 3A–C) confirmed the growth of highly interconnected ultrathin nanosheets of $MoFe_2S_{4-z}Se_z$ with thickness ≈4–5 nm and length ≈40–60 nm (calculated from the FE-SEM images). The TEM images also witnessed the growth of the expected sheet structure (Figure 3D). The high-resolution TEM image of $MoFe_2S_{4-z}Se_z$ (Figure 3E) and the corresponding fast Fourier transform (FFT) (inset) and IFFT (Figure 3F) showed fringes with lattice spacing ≈0.31 nm, assigned to the (311) plane of the $MoFe_2S_{4-z}Se_z$ indicating the formation of the same.[21–26] The SAED of the $MoFe_2S_{4-z}Se_z$ (Figure S3B, Supporting Information) also showed a diffraction pattern corresponding to the (400) and (111) planes of iron sulfide.[21–26] Elemental mapping of $MoFe_2S_{4-z}Se_z$ obtained from both TEM (Figure 3G) and FE-SEM (Figure S7, Supporting Information) showed the presence of all the constituent elements Fe, S, Mo, and Se apparently in equivalent ratio, and confirmed the formation of the $MoFe_2S_{4-z}Se_z$ ultrathin nanosheets.

The X-ray powder diffraction patterns of $MoFe_2S_{4-z}Se_z$ (Figure 2B) showed peaks at 2θ = 25.4°, 30.1°, 36.4°, 48.1°, and 52.4° corresponding to the (220), (311), (400), (511), and (440) planes (PDF No. 16-0713) confirming the formation of the same.[21–26] XPS analysis of $MoFe_2S_{4-z}Se_z$ in the rage 0-700 eV confirmed the presence of the specific peaks corresponding to Fe 2p, S 2p, Mo 3d, and Se 3d (Figure S8, Supporting Information). The analysis of the high-resolution XPS spectra of the individual components specifically concluded the formation of the $MoFe_2S_{4-z}Se_z$ (Figure 3H). De-convoluted high-resolution XPS spectrum of Fe 2p (Figure $3H_1$) showed the presence of the peaks at 706.7, 710.2, and 713.6 eV corresponding to Fe $2p_{3/2}$ and the peaks at 719, 724.3, and 731.7 eV corresponding to Fe $2p_{1/2}$.[21–26] The binding energy values are little higher in comparison to the bare iron sulfide due to the presence of higher electronegative metal Mo in the surroundings.[25,26] Figure $3H_2$ shows the high-resolution XPS peaks at 168.6, 163.0, 162.5, and 161.3 eV corresponding to the sulfate, S*SO_3, S $2p_{1/2}$, and S$2p_{3/2}$, respectively.[21–26] The peaks at 235.2, 232.3, and 229.8 eV (Figure $3H_3$) in the XPS spectrum of Mo 3d were observed due to Mo^{6+} $3d_{3/2}$, Mo^{4+} $3d_{3/2}$, and Mo^{4+} $3d_{5/2}$, respectively. The additional peak appeared at 226.5 eV is corresponding to S 2s.[10,13–18,21–26] The slight decrease in the binding energy was observed for the de-convoluted high-resolution peaks of the Mo 3d when compared to the pristine MoS_2. This is due to the presence of nearby Fe species, which has relatively lower electronegativity.[10,13–18,21–26] Figure $3H_4$ shows the presence of peaks at 57.1, 55.1, and 52.6 eV corresponding to the oxidized Se, $3d_{3/2}$, and $3d_{5/2}$, respectively.[21–26]

The highly porous nature of the ultrathin $MoFe_2S_{4-z}Se_z$ was confirmed by N_2 adsorption-desorption isotherm (Figure 2D), which showed a typical type IV hysteresis loop, indicating the mesoporous characteristics of the material with specific surface area of ≈48.5 m^2 g^{-1} and pore size of ≈6.1 nm (Figure 2D and Figure S2C, Supporting Information). The surface area and porosity of the present material is well compatible with the recently reported transition-metal chalcogenide based freestanding negative electrodes.[10,13–18,21–26]

2.2. Electrochemical Performance of the Materials in Three-Electrode Configurations

The electrochemical characterization of the individual freestanding electrodes was carried out in a standard three-electrode system using Ag/AgCl (sat.) and Pt foil as reference and counter electrodes, respectively. The expected pseudocapacitive materials grown on CC were used directly as working electrodes (1 cm × 1 cm) in 3M aqueous KOH electrolyte throughout the experiments. A pair of Faradaic redox peaks (**Figure 4**A) was observed in cyclic voltammetry (CV) curves in the range 0.1-0.5 V for all the materials, i.e., 1T-$Mn_xMo_{1-x}S_{2-y}$ Se_y, MoS_2, Mn-intercalated MoS_2, and Se-doped MoS_2, particularly because of the reversible redox reactions occurring at the electrodes involving the conversion of Mo^{2+}/Mo^{6+} and vice versa.[21–26] Due to the doping of Mn in the host system, it was anticipated that the redox reaction involving the conversion of Mn^{2+}/Mn^{3+} would also exist both in Mn-intercalated MoS_2 and 1T-$Mn_xMo_{1-x}S_{2-y}Se_y$, MoS_2.[21–26] However, the presence of such redox reaction could not be reflected in the CV curve due to the relatively low content of Mn in the host MoS_2 that resulted in masking of Mn^{2+}/Mn^{3+} redox peak by the dominant redox peak of the Mo^{2+}/Mo^{6+} redox couple present in the similar potential range.[21–33] The possible reactions taking place at the electrodes with the insertion of electrolytic solvated cations can be represented as: $MoS_2OH + OH^- \leftrightarrow MoS_2O + H_2O + e^-$ and $MnS_2 + OH^- \leftrightarrow MnS_2(OH^-)$; $MnS_2(OH^-) \leftrightarrow MnOS_{2+} H_2O + e^-$.[21–26] A sequential increment in the area enclosed by the CV profiles was observed as: MoS_2 < Se-doped MoS_2 (Se-MoS_2) < Mn-intercalated MoS_2 (Mn-MoS_2) < 1T-$Mn_xMo_{1-x}S_{2-y}Se_y$ (1T-Mn-Se-MoS_2) (Figure 4A). The intensity of the redox peaks was highest for 1T-$Mn_xMo_{1-x}S_{2-x}Se_x$ and the corresponding value was also significantly high when compared to the other materials under consideration. The observed trend indicated toward better redox kinetics for 1T-$Mn_xMo_{1-x}S_{2-x}Se_x$ was reflected in the calculated specific capacity values. The reasons behind such observations could be listed as: (i) improvement in the surface morphology, (ii) increase in the interlayer spacing, and (iii) enrichment of the highly conductive metallic 1T phase.[10–19,22–26]

The quantification of the charge-storage capability of the materials was done by interpreting the galvanostatic charge–discharge (GCD) profiles. Typically, all the materials showed battery-type trend in their profile characteristics with long redox region and this led to a longer discharge time (Figure 4B).[10–19,22–26] The maximum discharge time was observed for 1T-$Mn_xMo_{1-x}S_{2-y}Se_y$ (1T-Mn-Se-MoS_2) at a current density of 1 mA cm^{-2} (Figure 4B), which was also anticipated from the CV profiles (Figure 4A). Again, the discharge time followed the order: 1T-$Mn_xMo_{1-x}S_{2-y}Se_y$ (1T-Mn-Se-MoS_2; 1230 s) > Mn-intercalated MoS_2 (Mn-MoS_2; 820 s) > Se-doped MoS_2 (Se-MoS_2; 610 s) > MoS_2 (480 s) (Figure 4B). The electrochemical impedance spectroscopy (EIS) study (Figure 4C) reflected the significant improvement in the electrical conductivity and charge-transport kinetics in the 1T-$Mn_xMo_{1-x}S_{2-y}Se_y$ (1T-Mn-Se-MoS_2) compared to the other intermediate materials as ascertained from ESR.[10–19,22–26] The Nyquist plot (Figure 4C) represents charge-transfer resistance (R_{ct}) numbers in the following order: 1T-$Mn_xMo_{1-x}S_{2-y}Se_y$ (1T-Mn-Se-MoS_2) < Mn intercalated MoS_2 (Mn-MoS_2) < Se-doped MoS_2 (Se-MoS_2) < MoS_2.

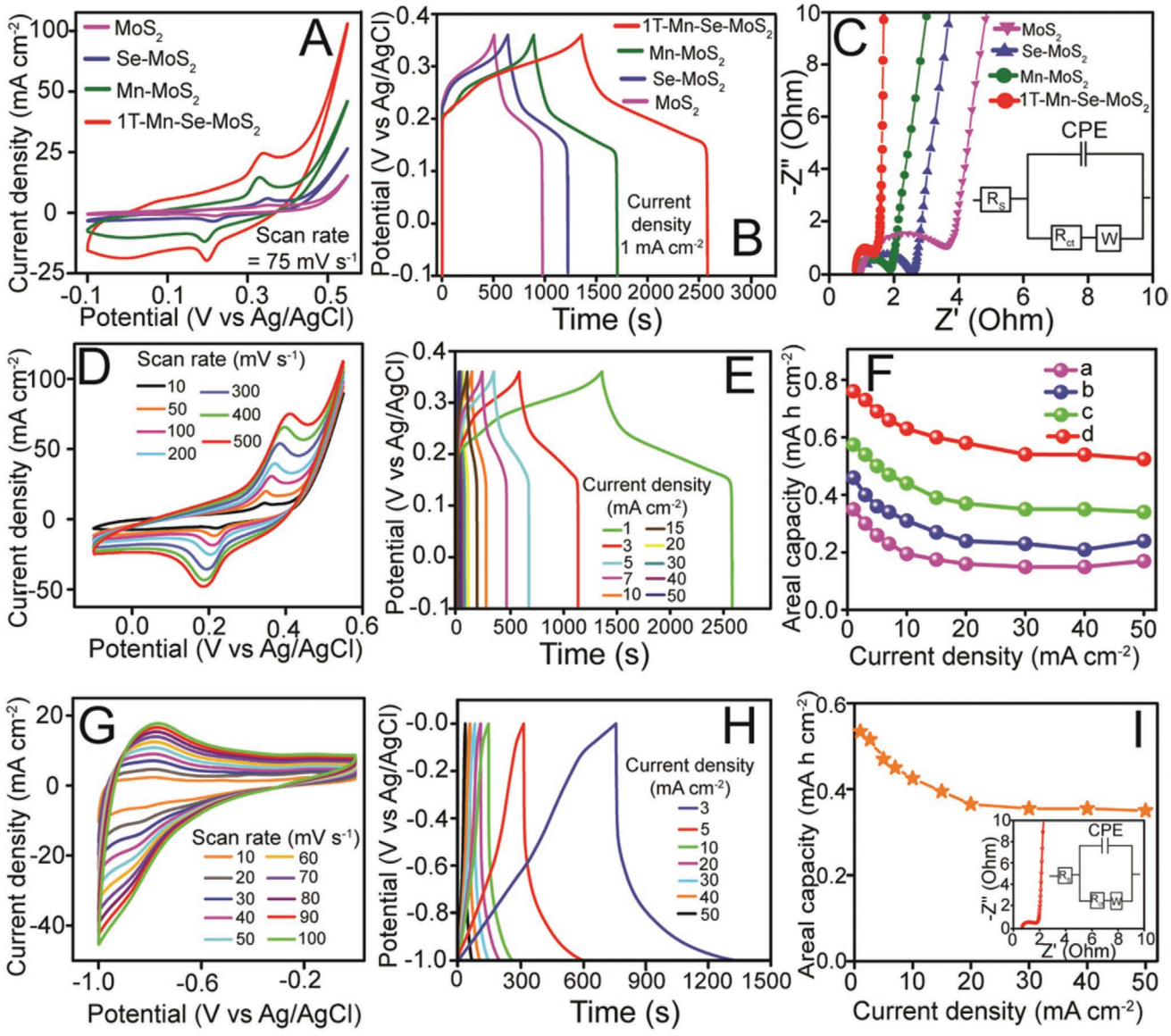

Figure 4. A) CV curves of MoS_2, Se-doped MoS_2 (Se-MoS_2), Mn-intercalated MoS_2 (Mn-MoS_2), and 1T-$Mn_xMo_{1-x}S_{2-y}Se_y$ (1T-Mn-Se-MoS_2) nanostructures at a fixed scan rate of 75 mV s^{-1}. B) GCD curves of MoS_2, Se-doped MoS_2 (Se-MoS_2), Mn-intercalated MoS_2 (Mn-MoS_2), and 1T-$Mn_xMo_{1-x}S_{2-y}Se_y$ (1T-Mn-Se-MoS_2) nanosheet arrays at a fixed current density of 1 mA cm^{-2}. C) EIS spectra of MoS_2, Se-doped MoS_2 (Se-MoS_2), Mn-intercalated MoS_2 (Mn-MoS_2), and 1T-$Mn_xMo_{1-x}S_{2-y}Se_y$ (1T-Mn-Se-MoS_2) nanostructures. D) CV curves of 1T-$Mn_xMo_{1-x}S_{2-y}Se_y$ nanosheets at different scan rates. E) GCD curves of 1T-$Mn_xMo_{1-x}S_{2-y}Se_y$ nanosheets at different current densities. F) Plot of specific capacities versus current densities of a) MoS_2, b) Se-doped MoS_2, c) Mn-intercalated MoS_2, and d) 1T-$Mn_xMo_{1-x}S_{2-y}Se_y$ nanostructures. G) CV curves of $MoFe_2S_{4-z}Se_z$ nanosheets at different scan rates. H) GCD curves of $MoFe_2S_{4-z}Se_z$ nanosheets at different current densities. I) Plot of specific capacities versus current densities of $MoFe_2S_{4-z}Se_z$ nanosheets and EIS spectrum of the same (inset).

This clearly indicates that enrichment of the 1T phase, increase in interlayer spacing, and improvement in the surface morphology has significantly improved the ion/charge-transport kinetics at the interface of the electrode and the electrolyte in 1T-$Mn_xMo_{1-x}S_{2-y}Se_y$ compared to the others.[10–19,22–24,26]

Later, the CV characteristics of the 1T-$Mn_xMo_{1-x}S_{2-y}Se_y$, at different scan rates from 10 to 500 mV s^{-1}, showed very well retention in the shape of the curve, and distinguishable anodic and cathodic peaks (Figure 4D) indicated excellent electron conduction with ultrahigh rate capability.[10,13–18] Further, the charge-storage mechanism and capacitive contribution of the 1T-$Mn_xMo_{1-x}S_{2-y}Se_y$ electrode was investigated according to the formula $i = av^b$, where i represents current, v is the scan rate, and a and b are constants.[21–33] For electric double layer capacitance (EDLC), $b = 1$ and for diffusion-controlled process, $b = 1/2$.[21–33] Based on this concept, we can represent the above equation as: $i\ (V) = k_1v + k_2v^{1/2}$, where i is the peak current, k_1 and k_2 are constants and numerically equal to the slope ≈0.7 mA cm^{-2}/mV s^{-1} and intercept ≈4.9 mA cm^{-2}/(mV s^{-1})$^{1/2}$ of the plot $v^{1/2}$ versus $i(V)/v^{1/2}$ (Figure S9A, Supporting Information).[21–33] Knowing k_1 and k_2 values, the capacitive contribution (k_1v) and the diffusive

contribution ($k_2\nu^{1/2}$) are calculated at different scan rates, as shown in Figure S9B (Supporting Information). It is observed that in all the different scan rates, the capacitive contributions are significantly lower than the diffusive contributions (Figure S9B, Supporting Information). This indicates that the charge storage mechanism of the 1T-$Mn_xMo_{1-x}S_{2-y}Se_y$ electrode is dominated by diffusion controlled process.[21–33] The highly ordered linear relationship observed for both the redox peaks upon varying scan rates also indicated that the Faradaic redox reactions were diffusion controlled.[10,13–18] GCD curves for the 1T-$Mn_xMo_{1-x}S_{2-y}Se_y$ at different current densities (1 to 50 mA cm^{-2}) showed a near symmetric nature in charging and discharging time (Figure 4E) justifying the excellent coulombic efficiency of the electrode.[10–19,22–26] The highest potential window in the GCD curve at current density 1 mA cm^{-2} for MoS_2 was found to be ≈0.36 V (similar to the other reported literature of MoS_2)[24] and remained similar for 1T-$Mn_xMo_{1-x}S_{2-y}Se_y$ too (Figure 4E).

Following GCD, the areal and specific capacity for all the materials was calculated at different current densities. The areal capacity value for 1T-$Mn_xMo_{1-x}S_{2-y}Se_y$ at 1 mA cm^{-2} was ≈0.76 mA h cm^{-2}, which is much higher than of Mn intercalated MoS_2 (≈0.574 mA h cm^{-2}), Se-doped MoS_2 (≈0.46 mA h cm^{-2}), and MoS_2 (≈0.35 mA h cm^{-2}) (Figure 4F). The trend indicated toward the superior nature of the 1T-$Mn_xMo_{1-x}S_{2-y}Se_y$ to act as the host for the incoming ions. The calculated specific capacity for 1T-$Mn_xMo_{1-x}S_{2-y}Se_y$ predominantly showed very high specific capacity of ≈288 mA h g^{-1} compared to that of the other intermediate materials Mn intercalated MoS_2 (≈172 mA h g^{-1}), Se-doped MoS_2 (≈144 mA h cm^{-2}), and MoS_2 (≈110 mA h cm^{-2}), respectively. Moreover, 81% capacity retention was also observed at a very high current density of 50 mA cm^{-2} for 1T-$Mn_xMo_{1-x}S_{2-y}Se_y$ indicating excellent rate capability for the electrode material.[10–19,22–26] In addition to that, the long-term electrochemical stability of the 1T-$Mn_xMo_{1-x}S_{2-y}Se_y$ electrode was also tested following consecutive charge–discharge cycles; the electrode showed 88.6% retention in the initial capacity even after 10 000 successive GCD cycles at a current density of 50 mA cm^{-2}, confirming the stable nature of the material for prolong use (Figure S10A, Supporting Information).[10–19,22–26]

After the optimization of the positive electrode, the detailed electrochemical characterization was performed for the free-standing negative electrode, i.e., $MoFe_2S_{4-z}Se_z$ with ultrathin sheet morphology exhibiting high surface area and porosity. The electrochemical measurements were performed in the same 3 M KOH aqueous electrolytic solution. The CV curve of the $MoFe_2S_{4-z}Se_z$ electrode collected in the operating window –1.0–0 V showed a predominantly battery-type nature supported by the Faradaic redox reactions (Figure 4G).[21–26] The CV curves showed electrochemical reversibility and no apparent change in the shape and the peak position was observed with the increment in scan rate from 10 to 100 mV s^{-1} (Figure 4G). This further justified the outstanding electrochemical processes at the electrode, and the reactions were again diffusion controlled.[21–26] The possible Faradaic reaction is involved the inter-transition in the valences of the Fe^{3+}/Fe^{2+} redox couple.[21–26] The GCD profiles for $MoFe_2S_{4-z}Se_z$ at different current densities (1–50 mA cm^{-2}) showed a close symmetric nature in the charging and discharging trend (Figure 4H) indicating excellent coulombic efficiency, which is highly desirable for an excellent electrode material in supercapacitors. Subsequently, the areal and specific capacity of the electrode materials obtained from the GCD characteristics was ≈0.534 mA h cm^{-2} and ≈218 mA h g^{-1} at 1 mA cm^{-2}. Moreover, we have tested the cyclic stability of the $MoFe_2S_{4-z}Se_z$ electrode for 10 000 consecutive GCD cycles at a current density of 50 mA cm^{-2}. The result showed an impressive 86.2% capacity retention (Figure S10B, Supporting Information), indicating excellent stability of the electrode for long-term steady operation. An impressive capacity retention of ≈69% in areal capacity was also observed when the current density was increased to 50 times of the initial value (Figure 4F), which proved that the material possesses excellent rate capability, which was associated with the high surface area and the extent of surface redox reactions taking place at the electrode.[10–28]

2.3. Flexible and Solid-State 1T-$Mn_xMo_{1-x}S_{2-y}Se_y$//$MoFe_2S_{4-z}Se_z$ Asymmetric Supercapacitor

To explore the practical utility of the as-fabricated individual positive and negative electrodes for the next-generation wearable and flexible electronics, a solid-state flexible ASC was fabricated. The individual electrodes were clubbed using a poly(vinyl alcohol) (PVA)/KOH gel electrolyte sandwiched between them. On the basis of the three-electrode performance of the respective electrodes, the mass ratio of the positive to the negative electrode was kept at ≈0.7 for the fabrication of the FS-ASC. To optimize the best operating potential range for the FS-ASC, CV curves were collected in different potential windows, at a fixed scan rate. Within the potential window of 0-1.5 V or 0-1.6 V distinct redox peaks were emerged due to the Faradic redox reactions related to the 1T-$Mn_xMo_{1-x}S_{2-y}Se_y$ and $MoFe_2S_{4-z}Se_z$ electrodes (Figure S11A, Supporting Information). Beyond 1.6 V, the oxygen evolution reaction started to appear (Figure S11A, Supporting Information), which confirmed that the fabricated ASC was limited to ≈1.6 V in which the electrochemical analysis was carried out.[10–27] The GCD profiles collected in different potential windows also showed a significant increase in the areal capacity with an increase in the potential window from 0-1.5 V to 0-1.6 V, as estimated from the area under the discharging curve (Figure S11B, Supporting Information). Although, further increase in the potential window to 1.7 V showed a significant degradation in the columbic efficiency (Figure S11B, Supporting Information) of the device. Thus, 1.6 V was finalized for the device characterization in order to achieve maximum energy density and sufficient power density, without compromising the columbic efficiency.[10–33]

The CV curves of FS-ASC at different scan rates starting from 10 to 100 mV s^{-1} did not show any significant alteration in the shape (**Figure 5**A). This proved that the redox peaks were dominant even at higher scan rates and the exceptional power density was expected from the FS-ASC (Figure 5A).[10–27] The results also indicated toward the reversible and fast electron transport properties of the device. GCD curves at different current densities from 3 to 50 mA cm^{-2} of the FS-ASC, within the potential window of 0–1.6 V, exhibited close symmetric nature

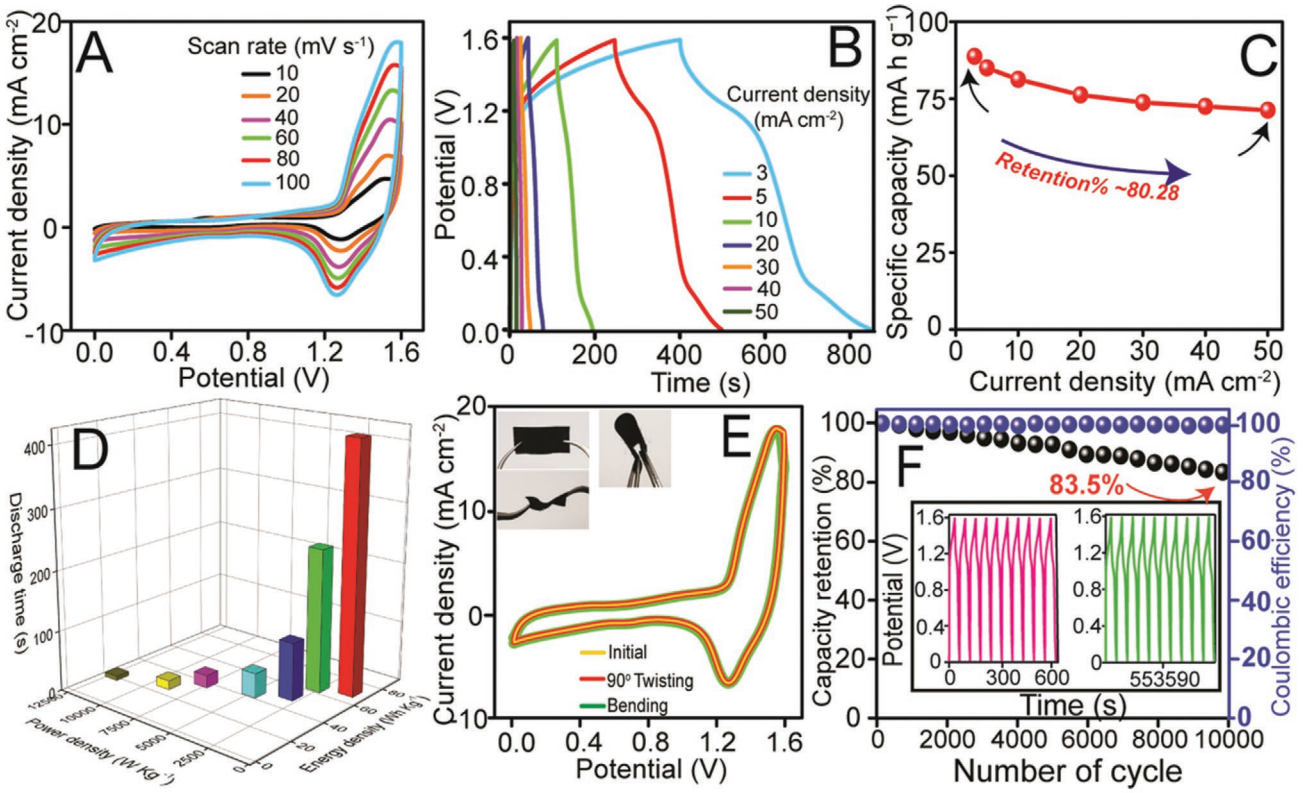

Figure 5. A) CV curves of 1T-$Mn_xMo_{1-x}S_{2-y}Se_y$//$MoFe_2S_{4-z}Se_z$ FS-ASC device at different scan rates. B) GCD curves of 1T-$Mn_xMo_{1-x}S_{2-y}Se_y$//$MoFe_2S_{4-z}Se_z$ FS-ASC device at different current densities. C) Plot of specific capacities versus current densities of the FS-ASC, showing a retention of 80.3% specific capacity even at very high current density of 50 mA cm^{-2}. D) The plot of discharge time versus energy density versus power density of the 1T-$Mn_xMo_{1-x}S_{2-y}Se_y$//$MoFe_2S_{4-z}Se_z$ FS-ASC. E) CV curve of the 1T-$Mn_xMo_{1-x}S_{2-y}Se_y$//$MoFe_2S_{4-z}Se_z$ FS-ASC after bending and twisting, showing no significant change in the nature of the curve; inset: digital photograph of bending and twisting of the 1T-$Mn_xMo_{1-x}S_{2-y}Se_y$//$MoFe_2S_{4-z}Se_z$ FS-ASC. F) Cyclic GCD performance of FS-ASC; inset: corresponding first and last ten cycles showing retention of 83.5% charge storing ability even after 10 000 cycles.

demonstrating the continuity in the redox reactions and their effectiveness at higher currents (Figure 5B).[10–27] The EIS of the FS-ASC was also obtained and represented in Figure S12 (Supporting Information). The Nyquist plot showed very low solution resistance (R_s, 0.97 Ω) and charge-transfer resistance (R_{ct}, 0.88 Ω) indicating excellent electrical conductivity of the FS-ASC.[10–33]

FS-ASC showed very high specific capacity of 91, 86, 82, 79, 75, and 73 mA h g^{-1} at current density of 3, 5, 10, 20, 30, 40, and 50 mA cm^{-2}, respectively, as calculated from the discharge curves (Figure 5C). The specific capacity retention of ≈80% was observed even at very high currents of 50 mA cm^{-2} exhibiting excellent rate capability of the device (Figure 5C). The general trend of decrement in capacity with increasing current density appears due to the limitation of the Faradaic redox reactions at the electrodes surface and decreased accessibility of the incoming ions on the electrode surface. The energy density and power density of the FS-ASC were calculated from the discharge profiles and are represented in the Ragone plot (Figure 5D). FS-ASC, in the present study, showed a high energy density of 69.1 Wh kg^{-1} at a power density of 985 W kg^{-1}, which could be considered as relatively high among the contemporary reports of various reported flexible supercapacitors (Table S1, Supporting Information).[10–27] With the increase in the power density, the FS-ASC showed substantial retention of the energy density and achieved a value of 21.2 Wh kg^{-1} at a significantly high power density of 12.1 kW kg^{-1}.

To test the robust flexible nature of the device, the CV curves were collected after bending and twisting the device. The results showed no significant change in the CV curve after successive bending or twisting (Figure 5E) establishing the FS-ASC as a true flexible device for the future wearable and foldable devices.[10–27] The cyclic stability of the supercapacitor is another important factor concerning its industrial utility. The present FS-ASC showed ultralong cyclic stability, as shown in Figure 5F. The results represented retentions of 97.2%, 92.1%, and 83.5% in the initial capacity after 2000, 5000, and 10 000 cycles of subsequent charge and discharge at current density 25 mA cm^{-2}. The superior performance of the FS-ASC could be ascribed to the improvement in the electronic character following the enactment of the 1T phase, formation of the 3D hierarchical nanosheet structure, and increase in the interlayer spacing with high porosity of the individual electrodes. These characteristics established the high operational potential of the current device with exceptional utility in power electronics.[10–33]

3. Conclusion

In summary, we have reported a high-performance flexible and solid state asymmetric supercapacitor based on the enrichment of the 1T phase of the MoS_2 and simultaneous doping of Mn and Se in a hierarchical nanosheet structure as the positive electrode and Mo and Se co-doped Fe_3S_4 ultrathin nanosheet as the negative electrode. The individual electrodes showed better performance than the contemporary reports equipped with synergistic behavior. This synergistic charge-storage performance in both electrode materials was expected due to the formation of highly ordered ultrathin nanosheet arrays, increase in interlayer spacing, and the stabilization of the metallic 1T phase of MoS_2, simultaneously. The flexible and solid-state asymmetric supercapacitor developed based on these two electrodes showed a high energy density of 69.1 Wh kg^{-1} at a power density of 0.985 kW kg^{-1}, along with ultralong cyclic stability of 83.5% capacity conservation after 10 000 cycles. The flexibility test of the device also showed nearly similar performance without any impairment. Thus, the present study proposes a flexible high-performance solid-state asymmetric supercapacitor and also opens up a novel dimension for the fabrication of new energy-storage materials. These materials have immense potential to exhibit high specific and areal capacity following the enrichment of the metastable but high conducting phase and manipulating the morphology by co-doping of metals and nonmetals in the host transition-metal chalcogenides.

4. Experimental Section

Fabrication of Flexible Positive Electrode: For the fabrication of the positive electrode, at first sodium molybdate dihydrate ($Na_2MoO_4.2H_2O$) and manganese (II) acetate were mixed in 9:1 molar ratio in a culture tube. Then 25 mL of deionized (DI) water was added to it and sonicated until a transparent solution was appeared. After that, 6 mmol of L-cysteine and 0.5 mmol of sodium selenide were added to it and again sonicated for 20 min. The solution was then transferred to a 100 mL beaker and 25 mL more DI water was added to it and stirred using Teflon-coated magnetic bar for 1 h. Finally, the solution was transferred to a 100 mL Teflon-lined autoclave, a clean carbon cloth was dipped into it, and then incubated at 180 °C for 14 h. After completion of the reaction the carbon cloth was taken out, washed with ethanol and water many times, and then dried at 60 °C for 24 h. The dried carbon cloth was kept for further experiments.[8,15,18,24]

Fabrication of the Flexible Negative Electrode: For the fabrication of the negative electrode iron (III) nitrate nonahydrate ($Fe(NO_3)_3,9H_2O$) and $Na_2MoO_4.2H_2O$ were mixed in 2:1 molar ratio with 25 mL DI water following sonication. After that, 6 mmol of L-cysteine and 0.5 mmol of sodium selenide was added to it and then again sonicated for some time and the solution was then transferred to a 100 mL beaker. The solution was then stirred using Teflon-coated magnetic bar for 1 h followed by the addition of 25 mL extra DI water. Finally, the solution was transferred to a 100 mL Teflon-lined autoclave, a clean carbon cloth was dipped into it, and the hydrothermal reaction was performed at 180 °C for 14 h. The carbon cloth was then collected and washed several times with water and ethanol, and dried for further characterization.[21–26]

Electrochemical Characterization: Electrochemical performance was measured using CH660E (CH Instruments, Inc., USA) electrochemical workstation. In the three-electrode setup Pt foil was used as the counter electrodes and silver/silver chloride electrode was used as the reference electrode. 3M KOH was used as the electrolyte and the as-prepared material on carbon cloth was used as the working electrode (1 cm × 1 cm).[21–26]

Fabrication of Flexible Solid-State ASCs: FS-ASC was fabricated following the integration of both the electrodes 1T-$Mn_xMo_{1-x}S_{2-x}Se_x$ and $MoFe_2S_{4-x}Se_x$ using gel electrolyte. A 40 µm thick NKK TF40 was used as the separator and KOH-PVA as the gel electrolyte. In detail, 2 g of KOH and 3 g of PVA powder were mixed with 36 mL DI water and then stirred at 90 °C for 1 h to prepare the gel electrolyte. After the preparation of the electrolyte, the separator was dipped into it and the FS-ASCs was prepared by placing the separator sandwich between the two electrodes. The device was then sealed with tape and connected with copper wire for electrochemical characterization.[21–26]

Specific Capacity/Areal Capacity Calculation: Specific capacity (CS) and areal capacity (CA) were calculated using the following formula

$$CS = \frac{2I \times \int V\,dt}{mV} \tag{1}$$

$$CA = \frac{2I \times \int V\,dt}{AV} \tag{2}$$

where I is the current, m is the active mass, A is the area of the electrode, and $\int V dt$ is the area under the discharge curve.[21–26]

Energy Density and Power Density: Energy density (E) and power density (P) of the FS-ASCs were calculated using the following equations[21–26]

$$E = \frac{I \times \int V\,dt}{m \times 0.36} \tag{3}$$

$$P = \frac{E}{t} \times 3600 \tag{4}$$

where t is the discharge time and other parameters are the same as described above.[21–26]

Supporting Information

Supporting Information is available from the Wiley Online Library or from the author.

Acknowledgements

The authors acknowledge help from Dr. Jayaraman Balamurugan, Dr. Amit K. Das, Huu Tuan Le, Dr. Thanh Tuan Nguyen, Dr. Haradhan Kolya, and Chandan Chandru Gudal. This research was supported by the Basic Science Research Program (2017R1A2B3004917) through the National Research Foundation (NRF) funded by the Ministry of Science and ICT of the Republic of Korea.

Conflict of Interest

The authors declare no conflict of interest.

Keywords

1T MoS_2 nanosheets, Fe_3S_4 nanosheets, flexible supercapacitors, hierarchical nanosheets, solid-state

Received: March 14, 2020
Revised: April 7, 2020
Published online:

[1] P. Simon, Y. Gogotsi, B. Dunn, *Science* **2014**, *343*, 1210.
[2] Y. Shao, M. F. El-Kady, J. Sun, Y. Li, Q. Zhang, M. Zhu, H. Wang, B. Dunn, R. B. Kaner, *Chem. Rev.* **2018**, *118*, 9233.
[3] A. González, E. Goikolea, J. A. Barrena, R. Mysyk, *Renewable Sustainable Energy Rev.* **2016**, *58*, 1189.
[4] L. Dong, C. Xu, Y. Li, Z. H. Huang, F. Kang, Q. H. Yang, X. Zhao, *J. Mater. Chem. A* **2016**, *4*, 4659.
[5] D. P. Dubal, N. R. Chodankar, D. H. Kim, P. Gomez-Romero, *Chem. Soc. Rev.* **2018**, *47*, 2065.
[6] K. S. Kumar, N. Choudhary, Y. Jung, J. Thomas, *ACS Energy Lett.* **2018**, *3*, 482.
[7] X. Hu, W. Zhang, X. Liu, Y. Mei, Y. Huang, *Chem. Soc. Rev.* **2015**, *44*, 2376.
[8] W. J. Zhang, K. J. Huang, *Inorg. Chem. Front.* **2017**, *4*, 1602.
[9] T. Wang, S. Chen, H. Pang, H. Xue, Y. Yu, *Adv. Sci.* **2017**, *4*, 1600289.
[10] K. Leng, Z. Chen, X. Zhao, W. Tang, B. Tian, C. T. Nai, W. Zhou, K. P. Loh, *ACS Nano* **2016**, *10*, 9208.
[11] Y. C. Lin, D. O. Dumcenco, Y. S. Huang, K. Suenaga, *Nat. Nanotechnol.* **2014**, *9*, 391.
[12] Q. Tang, D. E. Jiang, *Chem. Mater.* **2015**, *27*, 3743.
[13] E. Er, H. L. Hou, A. Criado, J. Langer, M. Möller, N. Erk, L. M. Liz-Marzán, M. Prato, *Chem. Mater.* **2019**, *31*, 5725.
[14] K. Zhang, S. Feng, J. Wang, A. Azcatl, N. Lu, R. Addou, N. Wang, C. Zhou, J. Lerach, V. Bojan, M. J. Kim, L. Q. Chen, R. M. Wallace, M. Terrones, J. Zhu, J. A. Robinson, *Nano Lett.* **2015**, *15*, 6586.
[15] S. S. Singha, S. Rudra, S. Mondal, M. Pradhan, A. K. Nayak, B. Satpati, P. Pal, K. Das, A. Singha, *Electrochim. Acta* **2020**, *338*, 135815.
[16] P. Liu, J. Zhu, J. Zhang, P. Xi, K. Tao, D. Gao, D. Xue, *ACS Energy Lett.* **2017**, *2*, 745.
[17] S. Liu, Y. Yin, M. Wu, K. S. Hui, K. N. Hui, C. Y. Ouyang, S. C. Jun, *Small* **2019**, *15*, 1.
[18] C. Kanade, S. Arbuj, K. Kanade, K. S. Kim, G. Y. Yeom, T. Kim, B. Kale, *RSC Adv.* **2018**, *8*, 39749.
[19] H. P. Komsa, A. V. Krasheninnikov, *J. Phys. Chem. Lett.* **2012**, *3*, 3652.
[20] A. Sellam, R. N. Jenjeti, S. Sampath, *J. Phys. Chem. C* **2018**, *122*, 14186.
[21] C. Li, J. Balamurugan, N. H. Kim, J. H. Lee, *Adv. Energy Mater.* **2018**, *8*, 1.
[22] T. T. Nguyen, J. Balamurugan, V. Aravindan, N. H. Kim, J. H. Lee, *Chem. Mater.* **2019**, *31*, 4490.
[23] J. Balamurugan, T. T. Nguyen, V. Aravindan, N. H. Kim, S. H. Lee, J. H. Lee, *Nano Energy* **2019**, *65*, 103999.
[24] N. Feng, R. Meng, L. Zu, Y. Feng, C. Peng, J. Huang, G. Liu, B. Chen, J. Yang, *Nat. Commun.* **2019**, *10*, 1372.
[25] Q. Li, Q. Wei, W. Zuo, L. Huang, W. Luo, Q. An, V. O. Pelenovich, L. Mai, Q. Zhang, *Chem. Sci.* **2016**, *8*, 160.
[26] J. Balamurugan, C. Li, V. Aravindan, N. H. Kim, J. H. Lee, *Adv. Funct. Mater.* **2018**, *28*, 1.
[27] J. Liu, J. Wang, C. Xu, H. Jiang, C. Li, L. Zhang, J. Lin, Z. X. Shen, *Adv. Sci.* **2018**, *5*, 1700322.
[28] J. Balamurugan, T. T. Nguyen, V. Aravindan, N. H. Kim, J. H. Lee, *Adv. Funct. Mater.* **2018**, *28*, 1.
[29] J. Liu, M. Hu, J. Wang, P. Wang, Y. Feng, H. Wang, F. Cao, Z. Chen, Y. Huang, *Energy Technol.* **2019**, *7*, 1900293.
[30] Z. Pan, J. Yang, Y. Zhang, X. Gao, J. Wang, *J. Mater. Chem. A* **2020**, *8*, 6406.
[31] Z. Pan, J. Yang, Q. Zhang, M. Liu, Y. Hu, Z. Kou, N. Liu, X. Yang, X. Ding, H. Chen, J. Li, K. Zhang, Y. Qiu, Q. Li, J. Wang, Y. Zhang, *Adv. Energy Mater.* **2019**, *9*, 1802753.
[32] Z. Pan, J. Yang, L. Li, X. Gao, L. Kang, Y. Zhang, Q. Zhang, Z. Kou, T. Zhang, L. Wei, Y. Yao, J. Wang, *Energy Storage Mater.* **2020**, *25*, 124.
[33] S. Ramki, K. Pandi, S. M. Chen, Y. T. Ye, T. W. Chen, Q. Hao, *Int. J. Electrochem. Sci.* **2019**, *14*, 1069.

